Chemical Engineering Science 314 (2025) 121773

Contents lists available at ScienceDirect

Chemical Engineering Science

journal homepage: www.elsevier.com/locate/ces

Characterization of the lateral gas–solid flow in a circulating fluidized bed boiler using simple mathematical model based on CPFD simulation data

Manxia Shang [a,b], Ling Jiang [a], Li Zhao [b], Zhong Huang [a,b,c], Xiwei Ke [b,c,*],
Junfu Lyu [a,b,c,*]

[a] Key Laboratory for Thermal Science and Power Engineering of Ministry of Education, Tsinghua University, Beijing 100084, China
[b] Shanxi Research Institute of Huairou Laboratory, Taiyuan 030006, China
[c] Beijing Huairou Laboratory, Beijing 101499, China

ARTICLE INFO

Keywords:
Lateral gas–solid flow
Circulating fluidized bed
Lateral voidage
Particle lateral movement velocity
Computational particle fluid dynamics
Neural network

ABSTRACT

Operation safety, combustion efficiency, and pollutant emissions of circulating fluidized bed (CFB) boilers are significantly affected by the lateral gas–solid flow uniformity, which can be featured by the voidage (ε_g) as well as particle lateral movement velocity (u_p). To obtain abundant data to support quantitative analysis and modeling, the gas–solid flow details in a 170 t/h CFB boiler were numerically simulated using the computational particle fluid dynamics (CPFD) method, which has been validated by field test data. Based on the original simulation data set, simple models for the prediction of lateral profiles of ε_g and u_p were developed. In addition, both theoretical model and genetic algorithm-back propagation (GA-BP) neural network were applied to predict the lateral solids movement behavior. Results show that both two models exhibit excellent prediction accuracy with the coefficient of determination (R_2) exceeding 0.99. While the theoretical model derived from physical equations is relatively simple and has a clear physical meaning. All the simple models developed in this paper can be embedded into the overall CFB mathematical model framework, facilitating the comprehensive analysis of the operational characteristics for large-scale industrial CFB boilers.

1. Introduction

Circulating fluidized bed (CFB) combustion technology has seen widespread development in recent years due to its excellent fuel adaptability (e.g., low-carbon fuel blending such as biomass and solid waste), pollutant control capabilities, and load regulation characteristics. It has also gradually evolved toward higher parameters and larger capacities (Blaszczuk and Nowak, 2015; Krzywanski et al., 2015; Nowak, 2003; Cai et al., 2018).

However, as furnace size increases, the issue of lateral non-uniformity in CFB boilers has become more pronounced. CFB boilers are typically fed with fuel on one side. This inherent asymmetry in the structural layout leads to uneven fuel distribution, causing inhomogeneous heat transfer and combustion within different regions. As a result, issues such as heating surface wear and temperature deviation may arise (Song et al., 2018). Although the secondary air is mostly designed to be symmetrically fed into the furnace, the direction of the furnace depth is often up to several meters long, and due to the limited penetration depth of the secondary air, there will be some dead zones. Poor design can severely disrupt the internal circulation of solids at the furnace's bottom, further exacerbating the inhomogeneity of solids distribution (Koeninger et al., 2017; Namkung and Sang, 2000). Furthermore, in the context of the global energy transition and the future large-scale integration of renewable energy into the power grid, CFB boilers will often operate in a low-load state (Shang et al., 2024). Nevertheless, when the load is significantly reduced, the lateral non-uniformity will be further exacerbated due to the reduction of wind speed and circulating flow rate (Ke et al., 2022). The lateral non-uniformity directly impacts the operation safety, combustion efficiency, and pollutant emissions of CFB boilers (Krzywanski et al., 2015; Jin et al., 2021; Bayham et al., 2017; Scala, 2018). To ensure the safe and economical operation of CFB boilers, it is necessary to conduct in-depth research on the lateral non-uniformity.

Voidage (ε_g) and particle lateral movement velocity (u_p) are key parameters in studying of lateral uniformity. The former serves as the basis for CFB fluid flow and combustion calculations (Xu et al., 1999),

---

* Corresponding authors at: Shanxi Research Institute of Huairou Laboratory, Taiyuan 030006, China.
E-mail addresses: kexiwei@sxri.hrl.ac.cn (X. Ke), lvjf@mail.tsinghua.edu.cn (J. Lyu).

https://doi.org/10.1016/j.ces.2025.121773
Received 7 April 2025; Received in revised form 28 April 2025; Accepted 30 April 2025

Table 1
Measurements of the lateral voidage in circulating fluidized bed systems.

Authors	D_t (mm)	H_t (m)	D_p (μm)	ρ_p (kg/m^3)	Techniques
Weinstein et al., 1985	152	8.5	59	1460	X-ray cameraabsorptiometry
Hartge et al., 1988	400	8.4	85; 120	1500; 2600	Fiber optical probe
Tung et al., 1988	90	10.0	54	929	Fiber optical probe
Herb et al., 1989	150	10.0	68	1500	Capacitance probe
Zhang et al., 1991	32; 90; 300	2.8; 10.0; 12	54; 75; 42.8	929; 607; 2003	Fiber optical probe
Xu et al., 1999	90	11	54	929.5	Fiber optical probe
Xu et al., 2004	90	11	54	929.5	Fiber optical probe
Zhu et al., 2013	100	7.9	90	1500	Fiber optical probe
Hensler et al., 2016	190	11.3	69.1	1027	X-ray computed tomography
Weber et al., 2018	305	15.3	886	863	Electrical capacitance volume tomography
Xu et al., 2018	384	60	200	2660	Sampling tube

while the latter governs the dispersion characteristics of gas–solid and the lateral mass exchange flow rates in CFB (Farzaneh et al., 2011).

For the lateral voidage distribution, researchers have conducted extensive measurements (Table 1) and characterizations (Table 2) in fluidized bed systems. As early as 1986, Weinstein et al. (Weinstein et al., 1985) measured the lateral voidage in a fast fluidized bed using X-rays and found a dilute core with a dense region on the wall. To quantitatively describe the lateral voidage profiles, Tung et al. (Tung et al., 1988) carried out measurements in a riser, and proposed an empirical correlation. Zhang et al. (Zhang et al., 1991) conducted more extensive experiments in three different fast fluidized bed systems using fiber optic probes. They found that the lateral voidage depends solely on the average cross-sectional lateral voidage. A more comprehensive correlation was proposed, which has since been widely used. Xu et al. (Xu et al., 2004) validated this correlation and found it applicable only to the dilute phase continuous clustering flow. To obtain a suitable correlation for estimating the lateral voidage of the bubbling flow, Xu et al. (Xu et al., 2004) established a new correlation for the dense phase continuous bubbling flow. In Hensler et al.'s study (Hensler et al., 2016), the experimental data based on X-ray computed tomography were compared to the results calculated using classical correlations, revealing that the correlation proposed by Xu et al. had an evident deviation in predicting the solids concentration distribution in the central region of the riser.

It indicates that many classical lateral voidage correlations are based on experimental data from laboratory-scale risers. Furthermore, most reactors have a circular cross-section, and the riser's height-to-diameter ratio exceeds 15, making lateral voidage profiles highly influenced by the sidewall effect. However, industrial-scale CFB boilers have a square cross-section, and their geometric dimensions extend to tens of meters. In this context, the applicability of previous correlations remains uncertain and warrants further investigation.

For the particle lateral movement velocity, there are relatively few experimental and theoretical studies (Wei et al., 1998; Zhang and Arastoopour, 1995; Herbert et al., 1998; Zhu and Zhu, 2008; Pallarès and Johnsson, 2006; Zhou et al., 2024; Metzger et al., 2024). Pallarès and Johnsson (Pallarès and Johnsson, 2006) employed particle tracking techniques to investigate the mixing mechanism of fuel particles in a narrow "two-dimensional" fluidized bed (0.4 m × 2.15 m × 0.02 m). Zhou et al (Zhou et al., 2024) developed a magnetic tracer-tracking system for a pilot-scale pressurized fluidized bed system and predicted the real-time velocity of the particles. Metzger et al. (Metzger et al., 2024) used magnetic resonance imaging to study the hydrodynamics of the particulate phase in three-dimensional draft tube spout-fluid beds. Tribedi et al. (Tribedi et al., 2023) introduced the radioactive particle tracking technique to measure the movement of Geldart group B particles in a pilot plant scale CFB riser. Lateral distributions of solid velocity parameters such as mean velocity, root-mean-square velocity, and granular temperature were obtained.

Although there have been some experimental studies on u_p in fluidized bed systems, most focus on laboratory-scale CFB risers, with limited experimental data. There is a lack of research on the quantitative modeling of u_p.

For strongly nonlinear systems such as CFB, an overall mathematical model based on flow simplification is an effective tool for research. However, most of the simplified mathematical models focus only on the axial distribution of gas–solid flow and axial backmixing of solids, neglecting the lateral gas–solid flow characteristics. Werther and Gungor et al. recognized the importance of lateral uniformity and developed a two-dimensional CFB mathematical model (Kruse et al., 1995; Schoenfelder et al., 1996; Kruse and Werther, 1995; Gungor and Eskin,

Table 2
Correlations for the lateral voidage in circulating fluidized bed systems.

Authors	Correlations	Specifications
Tung et al., 1988	$\begin{cases} \varepsilon_g = \overline{\varepsilon}_g^{(r/R)^2+0.191}, & r/R\leqslant 0.75 \\ \varepsilon_g = \overline{\varepsilon}_g^{3.62(r/R)^{6.47}+0.191}, & r/R\geqslant 0.75 \end{cases}$	R: radius of the riser
Zhang et al., 1991	$\varepsilon_g = \overline{\varepsilon}_g^{3(r/R)^{11}+(r/R)^{2.5}+0.191}$	
Patience and Chaouki, 1996	$\varepsilon_g = -4\left(\overline{\varepsilon}_g^{0.4} - \overline{\varepsilon}_g\right)(r/R)^6 + \overline{\varepsilon}_g^{0.4}$	
Wei et al., 1998	$\frac{1-\varepsilon_g}{1-\overline{\varepsilon}_g} = 2.2 - \frac{2}{1+\exp(10\cdot r/R - 7.665)}, \quad 0.68 < \overline{\varepsilon}_g < 0.95$	
Xu et al., 2004	$\begin{cases} \varepsilon_g = \varepsilon_w(\varepsilon_0/\varepsilon_w)^{F(r)}, \overline{\varepsilon}_g < 0.75 \\ F(r) = 1.0 - 0.06(r/R) - 1.34(r/R)^2 + 2.65(r/R)^3 - 2.25(r/R)^4 \\ \varepsilon_g = \overline{\varepsilon}_g^{a(r/R)^{11}+(r/R)^{2.5}+b}, a = \ln\varepsilon_w/\ln\overline{\varepsilon}_g - 1 - b, b = \ln\varepsilon_0/\ln\overline{\varepsilon}_g, \overline{\varepsilon}_g > 0.75 \end{cases}$	ε_w: local voidage on the bed wall ε_0: local voidage at bed center
Issangya et al., 2005	$\varepsilon_g = \varepsilon_{mf} + \left(\overline{\varepsilon}_g - \varepsilon_{mf}\right)\overline{\varepsilon}_g^{-1.5+2.1(r/R)^{3.1}+5.0(r/R)^{8.8}}$	ε_{mf}: voidage in incipient fluidization
Zhu et al., 2013	$\begin{cases} \frac{1-\varepsilon_g}{1-\overline{\varepsilon}_g} = 1.264 - \frac{0.547}{1+\exp(6.783\cdot r/R - 4.525)}, & h/D_{ts}\leqslant 4.77 \\ \frac{1-\varepsilon_g}{1-\overline{\varepsilon}_g} = 1.456 - \frac{0.908}{1+\exp(6.898\cdot r/R - 4.721)}, & h/D_{ts} > 4.77 \end{cases}$	D_{ts}: diameter of the riser's bottom section

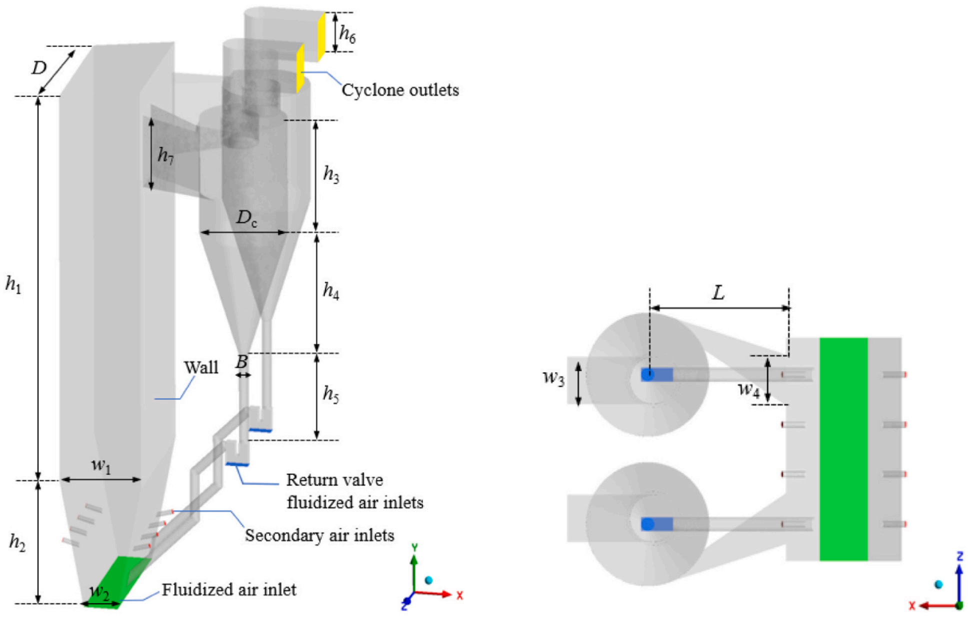

(a) **(b)**

Fig. 1. Geometric model of the CFB boiler: (a) CFB boiler; (b) Top view.

Table 3
Geometric dimensions of the CFB boiler.

Geometry	Symbol	Value (m)
Width of the entrance of the tapered segment	w_2	2.10
Width of the furnace	w_1	5.05
Depth of the furnace	D	9.73
Height of the tapered segment	h_2	7.94
Height of furnace	h_1	25.45
Height of the cyclone inlet	h_7	4.60
Width of the cyclone inlet	w_4	2.22
Length of the inlet duct	L	6.05
Diameter of the cylinder	D_c	5.38
Height of the cylinder	h_3	7.38
Height of the cone	h_4	7.87
Diameter of the lower outlet	B	0.60
Length of the lower outlet	h_5	5.67
Width of the cyclone outlet	w_3	2.06
Length of the cyclone outlet	h_6	2.61

2007; Gungor and Eskin, 2008). Nevertheless, in their models, the particle lateral diffusion coefficient was treated as a constant, and the lateral voidage correlations were based on limited experimental data from laboratory-scale risers. Whether these simplified approaches can be applied to the calculation of complex working conditions of CFB is questionable.

To carry out efficient and accurate parametric calculation of industrial CFB boilers, it is critical to establish a comprehensive two-dimensional model with accurate characterization of the lateral gas–solid flow. Industrial CFB boilers operate in a high-temperature and high-pressure environment, and there is a lack of effective measurement methods to obtain detailed flow field information. Given the constraints of cost, safety, and process analysis, advanced numerical experimental methods are necessary (Liu et al., 2023; Ma et al., 2023; Zhu et al., 2020). According to the multi-scale characteristics of gas–solid systems and the way of particle characterization, the simulation methods can be classified into particle-resolved direct numerical simulation (PR-DNS), Eulerian-Eulerian and Eulerian-Lagrangian methods (Shaffer et al., 2013). As a representative of the Euler-Lagrangian method, the

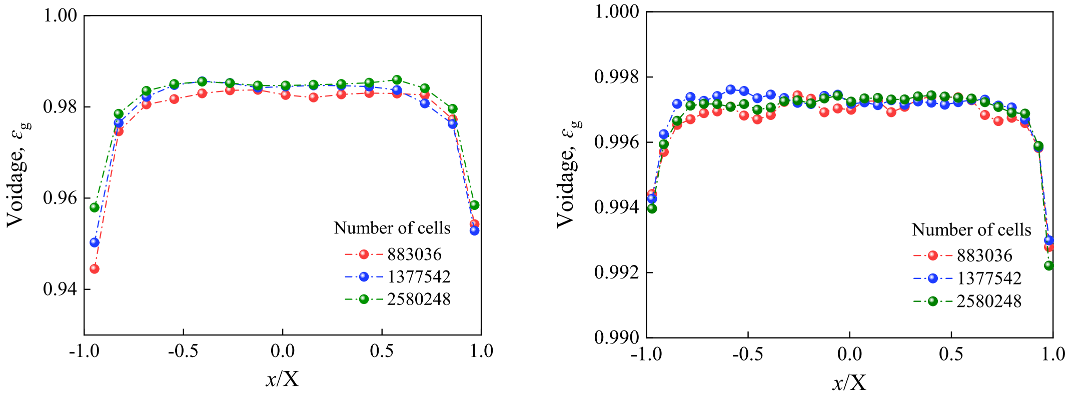

(a) ***h*=0.75 m** **(b)** ***h*=22.2 m**

Fig. 2. Results of the grid independence test.

Table 4
Summary of model input parameters.

Item	Parameter	Value
Simulation conditions	Initial bed inventory (m)	0.75
	Superficial gas velocity, u_g (m/s)	3.13; 3.40; 3.64; 3.83; 4.08; 4.31; 4.64
	Return valve fluidized air velocity (m/s)	0.35
	Secondary air mass flow rate (kg/s)	1.964; 2.360; 2.742; 3.070; 3.550; 3.905; 4.438
	Operating temperature (K)	1165.43
	Operating pressure (Pa)	102,371
	Outlet pressure (Pa)	99,950
Gas-solid physical property parameters	Gas density (kg/m^3)	0.3141
	Gas dynamic viscosity (Pa·s)	4.6508×10^{-5}
	Particle density (kg/m^3)	2450
	Close pack volume fraction	0.6
Particle-to-particle interaction	Maximum momentum redirection from collision (%)	40
	Particle normal stress model: Ps (Pa)	1
	Particle normal stress model: β	3
Particle-to-wall interaction	Normal-to-wall momentum retention	0.3
	Tangent-to-wall momentum retention	0.99
Solver settings	Maximum iterations of volume	10
	Residual of volume	1×10^{-7}
	Maximum iterations of pressure	2000
	Residual of pressure	1×10^{-8}
	Maximum iterations of velocity	50
	Residual of velocity	1×10^{-7}
	Initial time step	5×10^{-4}

computational particle fluid dynamics (CPFD) method uses the volume-averaged Navier-Stokes equations to describe the gas phase flow and tracks the motion of particle clouds as parcels. This method can simulate gas–solid flows in industrial-scale particle systems by incorporating solid phase stress and the concept of computational particles (Liu et al., 2023). In recent years, the feasibility and accuracy of this method in simulating gas–solid flow and combustion in fluidized beds have been demonstrated (Lee et al., 2022; Klimanek and Bigda, 2018; Yang et al., 2021; Huang et al., 2025). Bai et al. (Bai et al., 2023) developed a novel solar biomass method with the solid particle heat carrier, and the gasification in fluidized bed reactor was numerically studied with CPFD model, which indicated the enhancement of internal heat transfer and reaction kinetics.

An artificial neural network (ANN) is a computational model that simulates the operational characteristics of biological neural systems. In recent decades, ANN has been widely applied in many fields such as power and energy engineering, chemical engineering, and mechanical engineering due to its remarkable advantages in identifying complex nonlinear relationships between inputs and outputs (Singh et al., 2019; Valente et al., 2014; Sedighi et al., 2017). Genetic algorithm-back propagation (GA-BP) neural network combines the advantages of genetic algorithm and back propagation neural network with high prediction accuracy and efficiency, and is widely used in data prediction, pattern recognition, and other applications (Paliwal and Kumar, 2009; Chen et al., 2020; Ni and Yang, 2021).

In this study, the CPFD method verified with field test data was employed to perform a comprehensive numerical experiment on a 170 t/h CFB boiler. The lateral voidage and particle lateral movement velocity distributions in the furnace under different loads were obtained. Based on the original simulation data set from the CPFD method, simple mathematical models for describing the lateral distributions of ε_g and u_p were proposed. In addition, the GA-BP neural network was also applied to predict the u_p at different lateral positions, which is compared with the performance of theoretical model.

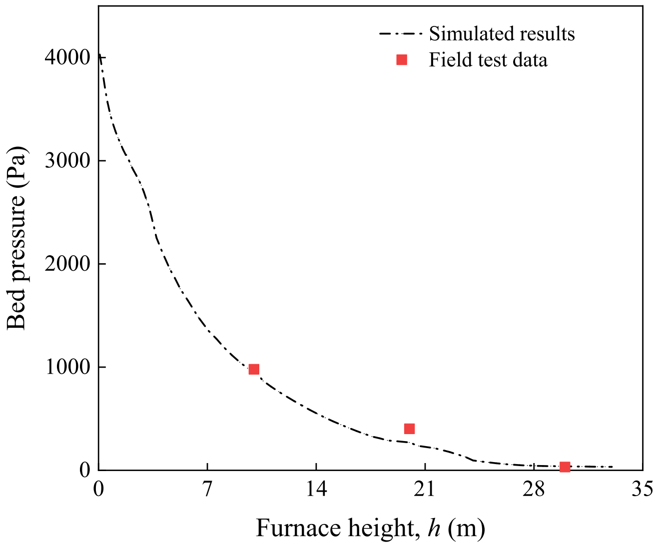

Fig. 4. Comparison of simulated results ($u_g = 4.08$ m/s) with field test data.

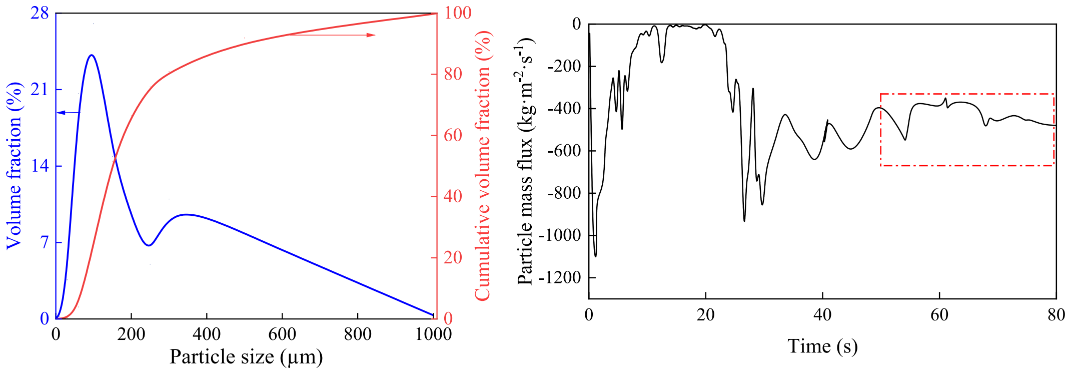

(a) **(b)**

Fig. 3. (a) Particle size distribution in calculation; (b) Particle mass flux at the lower outlet of the cyclone separator ($u_g = 4.08$ m/s).

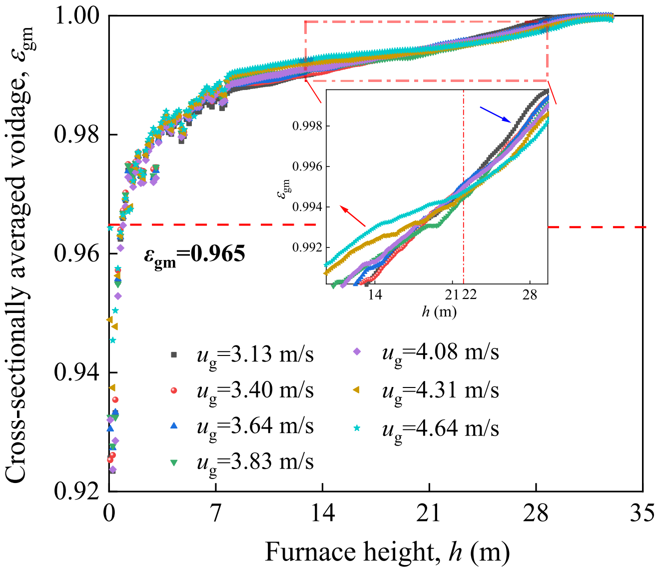

Fig. 5. Distribution of ε_{gm} along the furnace height at different superficial gas velocities.

2. CPFD simulation

2.1. Governing equations

The CPFD method was proposed by Dr. Dale Snide (Snider et al., 1998; Snider, 2001) based on the multiphase particle-in-cell numerical method (Andrews and O’Rourke, 1996). In this method, the gas phase is described as a continuum under the Eulerian framework. The turbulence model applied in the present work is the large-eddy simulation (LES). The continuity equation and momentum equations for the gas phase are shown as follows:

$$\frac{\partial(\rho_g\varepsilon_g)}{\partial t}+\nabla\cdot(\rho_g\varepsilon_g u_g)=0 \tag{1}$$

$$\frac{\partial(\rho_g\varepsilon_g u_g)}{\partial t}+\nabla\cdot(\rho_g\varepsilon_g u_g u_g) = -\nabla P+\rho_g\varepsilon_g g+\nabla\cdot(\varepsilon_g\tau_g)+F \tag{2}$$

where t represents time; ε_g, ρ_g, u_g, P, τ_g are the voidage, density, velocity, pressure, and stress tensor of the gas phase respectively; g is the gravitational acceleration; F represents the phase interaction force per unit volume, which can be calculated by Eq. (3):

$$F=\iiint f_p V_p\rho_p\left[D(u_g-u_p)-\frac{\nabla P}{\rho_p}\right]dV_p d\rho_p du_p \tag{3}$$

where f_p is the particle distribution function; V_p, ρ_p, and u_p are the volume, density, and velocity of the particle phase respectively; D is the interphase drag function.

The particle phase is treated as the discrete phase. The trajectory of the particle is calculated using Newton’s equation of motion. The particle acceleration A_p is shown below:

$$A_p=\frac{du_p}{dt}=D(u_g-u_p)-\frac{\nabla P}{\rho_p}+g-\frac{\nabla\tau_p}{\varepsilon_p\rho_p} \tag{4}$$

where ε_p is the particle volume fraction, ε_p = 1-ε_g; τ_p is the particle normal stress. The model of τ_p in this work is the Harris & Crighton model (Harris and Crighton, 1994) as Eq. (5):

$$\tau_p=\frac{P_s\varepsilon_p^{\beta}}{\max\left[(\varepsilon_{cp}-\varepsilon_p),\zeta(1-\varepsilon_p)\right]} \tag{5}$$

where P_s is a positive constant, β is a constant with a recommended value between 2 and 5. ζ is a very small number to eliminate the

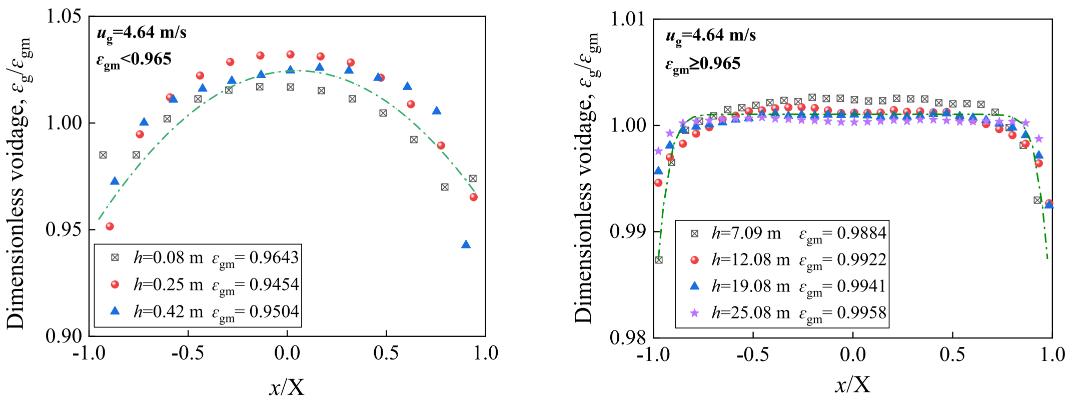

(a) **(b)**

Fig. 6. Lateral profiles of the dimensionless voidage on the cross-sections: (a) Distribution of $\varepsilon_g/\varepsilon_{gm}$ in the dense phase region; (b) Distribution of $\varepsilon_g/\varepsilon_{gm}$ in the dilute phase region.

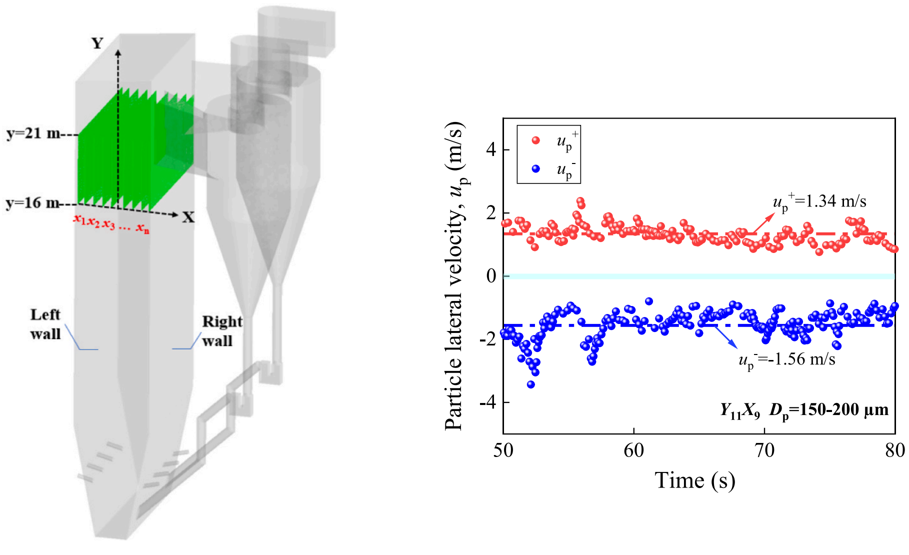

(a) **(b)**

Fig. 7. Distribution of particle lateral velocity on the monitoring surface $Y_{11}X_9$: (a) Monitoring surface settings; (b) Lateral velocity of particles with a size-cut group of 150–200 μm.

computation singularity.

The particle position x_p is calculated by Eq. (6):

$$\frac{dx_p}{dt} = u_p \tag{6}$$

2.2. Drag model

Drag force is the primary interaction force between the gas and solid phases. Calculating the drag force is crucial for determining the accuracy of the simulation. Various drag models have been developed, including Stokes (White, 1991), Wen-Yu (Wen and Yu, 1966), Ergun (Beetstra et al., 2007), and the Wen-Yu/Ergun hybrid model (Gidaspow, 1994). Among them, the Wen-Yu/Ergun mixed model applies to a wide range of particle concentrations, and its accuracy in predicting the gas–solid flow behavior in CFB has been verified in recent years (Ma et al., 2018; Yan et al., 2020). Therefore, the Wen-Yu/Ergun hybrid model was chosen in this study to calculate the drag force, as shown below:

$$D = \begin{cases} D_{\text{Wen-Yu}} = \dfrac{3}{8} C_d \dfrac{\rho_g}{\rho_p} \dfrac{|u_g - u_p|}{r_p}, & \varepsilon_p < 0.75\varepsilon_{cp} \\ \dfrac{\varepsilon_p - 0.75\varepsilon_{cp}}{0.85\varepsilon_{cp} - 0.75\varepsilon_{cp}} (D_{\text{Ergun}} - D_{\text{Wen-Yu}}) + D_{\text{Wen-Yu}}, & 0.75\varepsilon_{cp} < \varepsilon_p < 0.85\varepsilon_{cp} \\ D_{\text{Ergun}} = 0.5 \left[\dfrac{180\varepsilon_p}{(1-\varepsilon_p)\text{Re}_p} + 2 \right] \dfrac{\rho_g}{\rho_p} \dfrac{|u_g - u_p|}{r_p}, & \varepsilon_p > 0.85\varepsilon_{cp} \end{cases} \tag{7}$$

where $D_{\text{Wen-Yu}}$ is the drag function in the Wen-Yu drag model; D_{Ergun} is the drag function in the Ergun drag model; r_p is the particle radius; C_d is the drag coefficient, which can be calculated according to the Eq. (8):

$$C_d = \begin{cases} \dfrac{24}{\text{Re}_p} \varepsilon_g^{-2.65}, & \text{Re}_p < 0.5 \\ \dfrac{24}{\text{Re}_p} \left(1 + 0.15\text{Re}_p^{0.687}\right) \varepsilon_g^{-2.65}, & 0.5 \leqslant \text{Re}_p \leqslant 1000 \\ 0.44\varepsilon_g^{-2.65}, & \text{Re}_p > 1000 \end{cases} \tag{8}$$

where Re_p represents the particle Reynolds number, which can be calculated by Eq. (9):

$$\text{Re}_p = \frac{2\rho_g r_p |u_g - u_p|}{\mu_g} \tag{9}$$

where μ_g is the dynamic viscosity of the gas phase.

2.3. Geometry and mesh

The simulation was performed using the software Barracuda® 17.4.0. A 170t/h CFB boiler was modeled in a 1:1 ratio. The geometric model is shown in Fig. 1, and the main geometric parameters of the boiler are listed in Table 3.

The built-in grid division function of Barracuda was used to generate three different sizes of mesh in the Cartesian coordinate system: coarse mesh, medium mesh, and fine mesh. The corresponding effective mesh numbers were 883,036, 1,377,542, and 2,580,248, respectively. The lateral profiles of the voidage ε_g on the cross-sections with furnace heights of 0.75 m and 22.2 m under different meshes are shown in Fig. 2

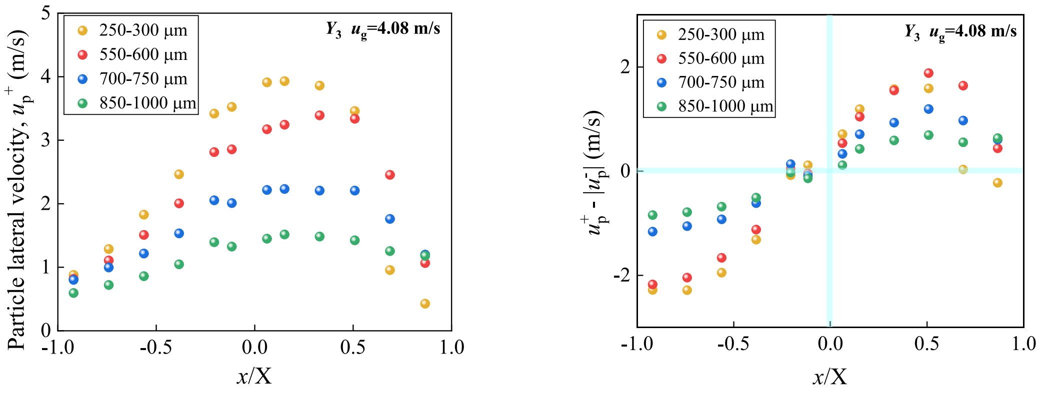

(a) u_p^+ on Y_3 surface (dense phase region)

(b) u_p^+-$|u_p^-|$ on Y_3 surface (dense phase region)

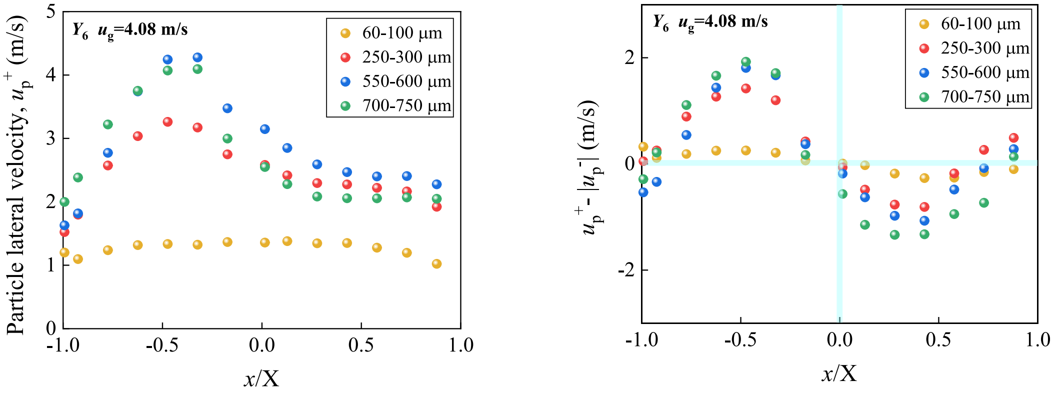

(c) u_p^+ on Y_6 surface (transition region)

(d) u_p^+-$|u_p^-|$ on Y_6 surface (transition region)

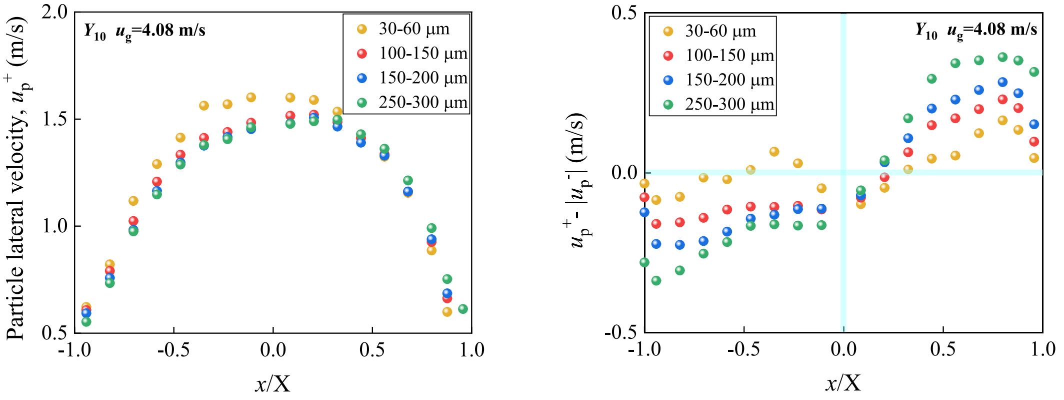

(e) u_p^+ on Y_{10} surface (dilute phase region)

(f) u_p^+-$|u_p^-|$ on Y_{10} surface (dilute phase region)

Fig. 8. Particle lateral velocity distribution in different regions: (a, b) for Y_3 surface in the dense phase region; (c, d) for Y_6 surface in the transition region; (e, f) for Y_{10} surface in the dilute phase region.

(a) and Fig. 2b respectively. It can be seen that the calculation results of the medium mesh are close to those of the fine mesh. Considering both the calculation accuracy and calculation cost, the medium mesh was chosen for the present study.

2.4. Boundary conditions

Fig. 1(a) demonstrates the setting of boundary conditions for the computational model. In the initial state, a certain height of solids is piled up at the bottom of the furnace. The air enters from the bottom of the furnace, the return valve, and the secondary air ports at specific velocities, respectively. A small number of fine particles escape through the separator outlet. Both fluidized air inlet and return valve fluidized air inlets are set as velocity inlets with specific velocities, as shown in Table 4; to make the calculation more stable, the secondary air inlets are set as mass flow inlets with specific mass flow rates; the cyclone outlets are set as pressure outlets with a fluid pressure of 99950 Pa. The particle size distribution in the calculation is shown in Fig. 3(a). The physical properties of the particles and gas, along with simulation conditions, solver settings, and other important input parameters are summarized in

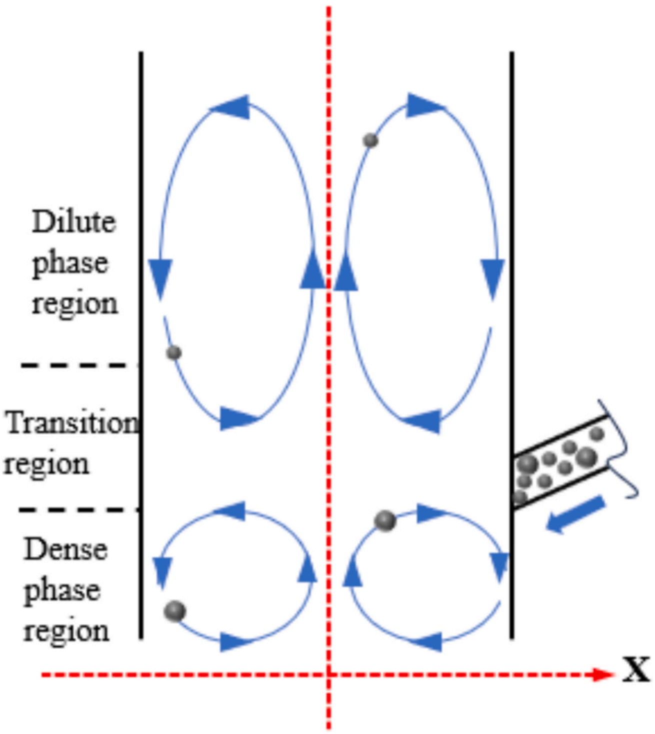

Fig. 9. Particle internal flow structures in different regions.

Table 4.

The total simulation time was 80 s. The initial time step was 5 × 10^{-4} s, and the Courant number CFL was set to 0.8–1.5. The particle mass flux at the lower outlet of the cyclone separator was monitored. As shown in Fig. 3(b), with the increase in the calculation time, the particle mass flux gradually reached stability after 45 s. Therefore, the average data from 50 s to 80 s were extracted as the calculation results under quasi-steady state.

2.5. *Model validation*

Before conducting the formal calculations, the measured bed pressure from the same industrial boiler was used to validate the CPFD model. Fig. 4 shows the comparison between the simulated values and the field test data. The CPFD-calculated bed pressure distribution is consistent with the measured data, verifying the reliability of the numerical model to some extent.

3. Characterization of lateral voidage distribution

3.1. *Numerically calculated distributions*

Numerous studies have shown that the lateral voidage profiles depend solely on the cross-sectionally averaged voidage $\varepsilon_{\mathrm{gm}}$ exclusively, and are independent of the operating conditions, solid properties, and fluidized bed diameter (Tung et al., 1988; Zhang et al., 1991; Xu et al., 2004). Fig. 5 exhibits the distribution of the cross-sectionally averaged voidage $\varepsilon_{\mathrm{gm}}$ along the furnace height at different superficial gas velocities. In the dense phase region, $\varepsilon_{\mathrm{gm}}$ is nearly constant, while in the dilute phase region, it exhibits an exponential growth with increasing furnace height. This distribution feature is consistent with many experimental results (Wong et al., 1992; Xu et al., 2018). With the increase of superficial gas velocity, $\varepsilon_{\mathrm{gm}}$ increases in the middle and lower regions of the furnace ($h < 22$ m), while it decreases in the upper region of the furnace.

The lateral profiles of the dimensionless voidage $\varepsilon_{\mathrm{g}}/\varepsilon_{\mathrm{gm}}$ on some specific cross-sections are presented in Fig. 6. Overall, the lateral profiles of $\varepsilon_{\mathrm{g}}/\varepsilon_{\mathrm{gm}}$ exhibit distinct distribution characteristics in the dense phase continuous bubbling flow region and the dilute phase continuous clustering flow region. In the dense phase region, the lateral voidage distribution follows the form of a parabola, consistent with previous research (Hartge et al., 1988; Tung et al., 1988; Zhang et al., 1991; Xu et al., 2004; Hensler et al., 2016). Different from it, in the dilute-phase region, although the lateral voidage remains high in the sidewall region, the distribution in the center is nearly flat, and a sharp transition between the sidewall and center regions occurs, which is different from the situation in previous studies (Zhang et al., 1991; Wei et al., 1998; Patience and Chaouki, 1996; Wang et al., 1998).

3.2. *Empirical correlation*

To quantitatively describe the lateral voidage profiles in a CFB, two distinct hydrodynamic regions, delineated at $\varepsilon_{\mathrm{gm}} = 0.965$, are identified based on the characteristic variations in the profiles. When $\varepsilon_{\mathrm{gm}} < 0.965$, the dense phase continuous bubbling flow prevails, which can be described by a polynomial. In contrast, when $\varepsilon_{\mathrm{gm}} \geq 0.965$, the voidage in the center region remains relatively constant, while the voidage in the side wall region decreases rapidly. Given this distribution feature, the Boltzmann distribution function is used for modeling. Based on the above analysis, the correlations for lateral voidage profiles are established as follows:

$$\varepsilon_{gm} < 0.965 \quad \frac{1-\varepsilon_{\mathrm{g}}}{1-\varepsilon_{\mathrm{gm}}} = \begin{cases} a\left(\frac{x}{\mathrm{X}}\right)^2 + b\left(\frac{x}{\mathrm{X}}\right) + c, & -1 \leqslant \frac{x}{\mathrm{X}} \leqslant 1 \\ a = 0.611 + e^{1.752\mathrm{Re}_{\mathrm{p}} - 8.425} \\ b = -0.05\mathrm{Re}_{\mathrm{p}}^3 + 0.50\mathrm{Re}_{\mathrm{p}}^2 - 1.577\mathrm{Re}_{\mathrm{p}} + 1.570 \\ c = 0.402 + \dfrac{0.267}{1 + e^{6.882\mathrm{Re}_{\mathrm{p}} - 30.278}} \end{cases} \tag{10}$$

$$\varepsilon_{gm} \geqslant 0.965 \quad \frac{1-\varepsilon_{\mathrm{g}}}{1-\varepsilon_{\mathrm{gm}}} = \begin{cases} 0.858 + \dfrac{5.651}{1 + e^{24.713\left(\frac{x}{\mathrm{X}}\right) + 24.830}}, & -1 \leqslant \frac{x}{\mathrm{X}} \leqslant 0 \\ 0.858 + \dfrac{5.651}{1 + e^{-24.713\left(\frac{x}{\mathrm{X}}\right) + 24.830}}, & 0 < \frac{x}{\mathrm{X}} \leqslant 1 \end{cases} \tag{11}$$

4. Characterization of particle lateral movement velocity

4.1. *Numerically calculated distributions*

To obtain the particle lateral velocity in the furnace, several monitoring surfaces were set up along the lateral direction at different furnace heights, denoted as Y_1, Y_2, …, Y_{n}, as shown in Fig. 7(a) (taking Y_{11} (16 m $\leq h \leq$ 21 m) as an example). For the lateral direction, monitoring surfaces are set up at different x-coordinate positions, denoted as $Y_{11}X_1$, $Y_{11}X_2$, …, $Y_{11}X_{\mathrm{n}}$. Following this approach, a total of 210 monitoring surfaces were set up along the furnace height and in the lateral direction. The coordinates of all monitoring surfaces are detailed in Table S1, Supplementary Material (SM). Particle information (unique particle ID, diameter, velocity vector, residence time, etc.) passing through the monitoring surfaces at different times is recorded, accordingly, the u_{p} distributions at various times and radii can be obtained. For convenience, the particles are divided into 19 size-cut groups according to the diameter, from 0 to 1050 μm.

Fig. 7(b) shows the u_{p} with a size-cut group of 150–200 μm passing through the surface $Y_{11}X_9$ within the time interval of 50–80 s. It can be seen that during this period, the u_{p} fluctuates, but most values are within a narrow range. Hence, in this paper, the average value of u_{p} in this period is used for the following analysis. Note that positive values

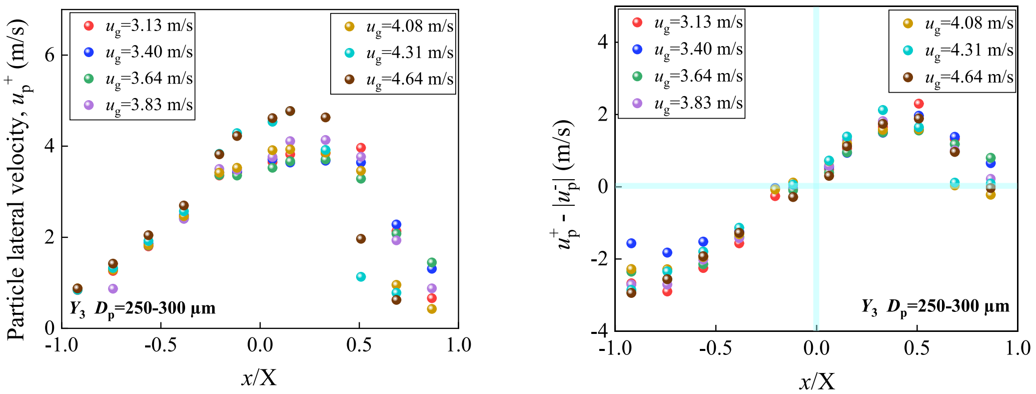

(a) u_p^+ **on** Y_3 **surface (dense phase region)** **(b)** u_p^+-$|u_p^-|$ **on** Y_3 **surface (dense phase region)**

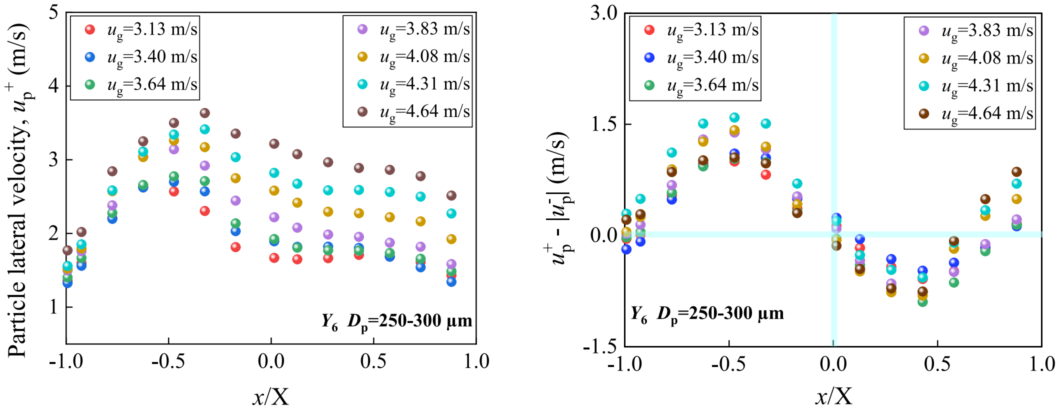

(c) u_p^+ **on** Y_6 **surface (transition region)** **(d)** u_p^+-$|u_p^-|$ **on** Y_6 **surface (transition region)**

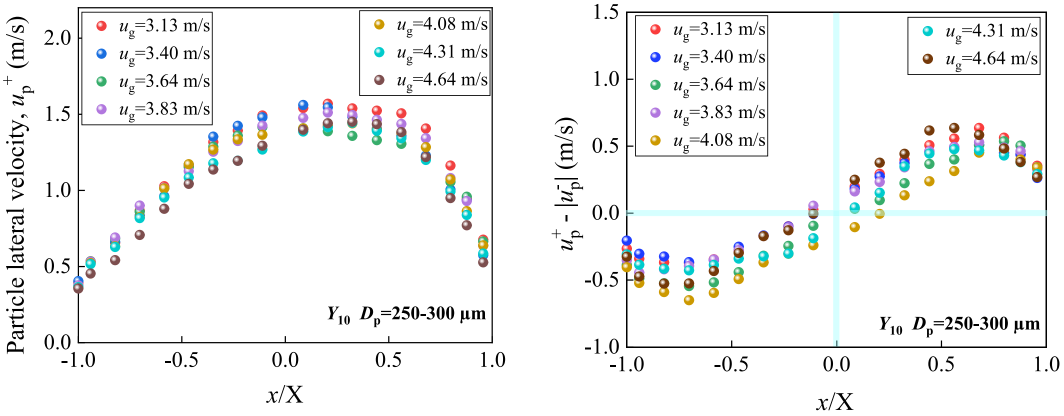

(e) u_p^+ **on** Y_{10} **surface (dilute phase region)** **(f)** u_p^+-$|u_p^-|$ **on** Y_{10} **surface (dilute phase region)**

Fig. 10. Particle lateral velocity distribution in different regions under different superficial gas velocities: (a, b) for Y_3 surface in the dense phase region; (c, d) for Y_6 surface in the transition region; (e, f) for Y_{10} surface in the dilute phase region.

indicate particles move in the positive direction of the X-axis.

Based on different distribution characteristics, the furnace can be divided into the dense phase region, the transition region, and the dilute phase region. Fig. 8 shows u_p distributions for particles with different sizes on some representative monitoring surfaces in different regions. Meanwhile, the velocity difference at the same lateral position (u_p^+-$|u_p^-|$) is also given. $x/X = 0$ represents the position of the vertical central surface inside the furnace and $x/X > 0$ points to the area near the right wall.

As shown in Fig. 8(a), in the dense phase region, u_p profiles for different size particles are roughly in the parabolic form. Fig. 8(b) further shows that, when $r/R > 0$, $u_p^+ > u_p^-$; when $r/R < 0$, $u_p^+ < u_p^-$. Namely, more particles tend to move laterally towards the wall, which leads to an increase in the particle concentration near the wall, and subsequently forms an internal solids circulation in the bottom bed, as shown in Fig. 9. It is observed that the distribution curves in Fig. 8(b) are not strictly centrally symmetric. This may be related to the fact that the particle return port is arranged on the right wall, that is, a large number

Table 5
Particle lateral movement velocity calculation model.

Region	Expression
$0.920 \leqslant \varepsilon_{gm} < 0.965$	$-u_g \ln\left(\left\|u_g - u_p^+\right\|\right) - u_p^+ = \left(\frac{8.091\varepsilon_g^{-2.65}}{r_p^2} \times 10^{-12} - \frac{0.00281\varepsilon_g^{-2.65}\left\|u_g - u_p^+\right\|^{0.687}}{r_p}\right)x - 0.96678$
	$u_g \ln\left(\left\|u_g - u_p^-\right\|\right) + u_p^- = \left(\frac{1.514\varepsilon_g^{-2.65}}{r_p^2} \times 10^{-11} - \frac{0.0038484\varepsilon_g^{-2.65}\left\|u_g - u_p^-\right\|^{0.687}}{r_p}\right)x - 0.82914$
$0.965 \leqslant \varepsilon_{gm} < 0.990$	$-u_g \ln\left(\left\|u_g - u_p^+\right\|\right) - u_p^+ = \left(\frac{2.157\varepsilon_g^{-2.65}}{r_p^2} \times 10^{-12} + \frac{0.000123\varepsilon_g^{-2.65}\left\|u_g - u_p^+\right\|^{0.687}}{r_p}\right)x - 1.61841$
	$u_g \ln\left(\left\|u_g - u_p^-\right\|\right) + u_p^- = \left(\frac{8.541\varepsilon_g^{-2.65}}{r_p^2} \times 10^{-12} - \frac{0.001524\varepsilon_g^{-2.65}\left\|u_g - u_p^-\right\|^{0.687}}{r_p}\right)x - 1.54211$
$\varepsilon_{gm} \geqslant 0.990$	$-u_g \ln\left(\left\|u_g - u_p^+\right\|\right) - u_p^+ = \left(\frac{8.116\varepsilon_g^{-2.65}}{r_p^2} \times 10^{-12} + \frac{0.00267\varepsilon_g^{-2.65}\left\|u_g - u_p^+\right\|^{0.687}}{r_p}\right)x - 0.65773$
	$u_g \ln\left(\left\|u_g - u_p^-\right\|\right) + u_p^- = \left(-\frac{8.685\varepsilon_g^{-2.65}}{r_p^2} \times 10^{-12} + \frac{0.002405\varepsilon_g^{-2.65}\left\|u_g - u_p^-\right\|^{0.687}}{r_p}\right)x - 0.7882$

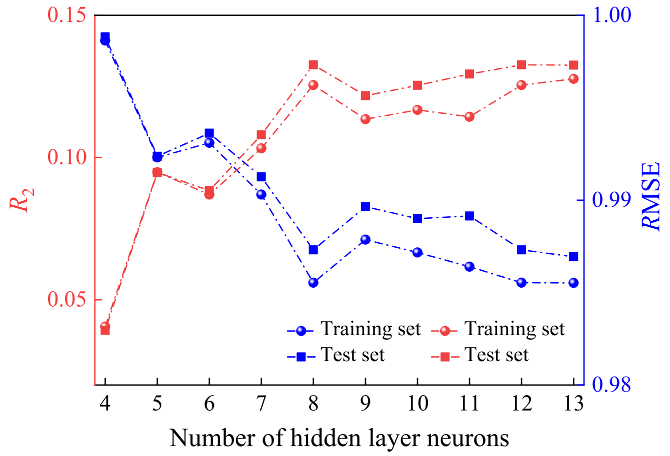

Fig. 11. RMSE and R_2 values of the test set and training set at different numbers of hidden layer neurons.

Table 6
Summary of the GA-BP neural network parameters.

Parameter	Description
ANN type	Single hidden layer feed forward neural network
Learning type	Supervised learning
Training algorithm	Levenberg-Marquardt
Number of input layer neurons	5
Number of hidden layer neurons	13
Number of output layer neurons	1
Activation function for the hidden layer	Logsig function
Activation function for the output layer	Tansig function
Maximum number of training epochs	20,000
Learning rate	0.0005
Population size	50
Maximum number of generations	50
Parameter of the selection function	0.09
Parameter of the cross function	2
Parameter of the variance function	[2 gen 3]

of particles rush into the furnace laterally from the right side, causing particles in the dense phase zone to tend to flow to the left.

Similar to the particle flow pattern in the dense phase region, a core-annulus flow pattern is formed in the dilute phase region. Namely, the particle flow rate towards the wall is greater than that towards the furnace center, resulting in the formation of a downward flow of dense-phase clusters near the wall. This phenomenon has also been confirmed by numerous experiments (Bai et al., 1995; Kim et al., 2004; Breault et al., 2020).

Different from the phenomena shown in the above two regions, in the transition region, the lateral movement direction of particles is opposite, demonstrating an obvious centripetal particle flow. This is because, under the influence of factors such as the central upward airflow and the secondary air injection, the particle clusters falling from the side walls are broken up and move inward and upward, until they enter the dilute phase region and re-agglomerate, thus forming a complete solid in-furnace circulation, as shown in Fig. 9.

Particle size and superficial gas velocity are key factors that control particle flow characteristics. As shown in Fig. 8, particles with different sizes exhibit varying velocity distributions. In the dilute phase region, the lateral velocity of fine particles is higher than that of coarse particles. Fine particles have a lower terminal velocity, making them more easily carried by the airflow. In the dense phase and transition regions, the situation is somewhat different. Due to the high particle concentration, the effect of inter-particle collisions on lateral velocity becomes significant. Coarse particles are more susceptible to collisions and thus become more active, resulting in a significantly higher lateral velocity compared to the dilute-phase region.

In this study, different boiler loads (boiler load ratio changes from 50 % to 110 %) are considered in the simulation, thus discussing the effects of superficial gas velocity on the fluid dynamics. Fig. 10 shows that, in the dense phase and transition regions, the higher the superficial gas velocity, the greater the gas's ability to carry particles, resulting in a general increase in u_p. Nevertheless, in the dilute phase region, at high superficial gas velocities, such as $u_g = 4.64$ m/s, u_p is slightly lower than that at relatively lower superficial gas velocity.

Other than particle size and gas velocity, some other factors, such as solid suspension concentration, also have significant impacts on the u_p distribution (Parssinen and Zhu, 2001). It can be seen that there are numerous interrelated influencing factors for u_p. Different from the description of voidage profiles, it is very difficult to accurately estimate the u_p value at any position in the furnace under various conditions using a unified correlation equation. Therefore, this paper attempts two technical approaches respectively, namely physical equation derivation

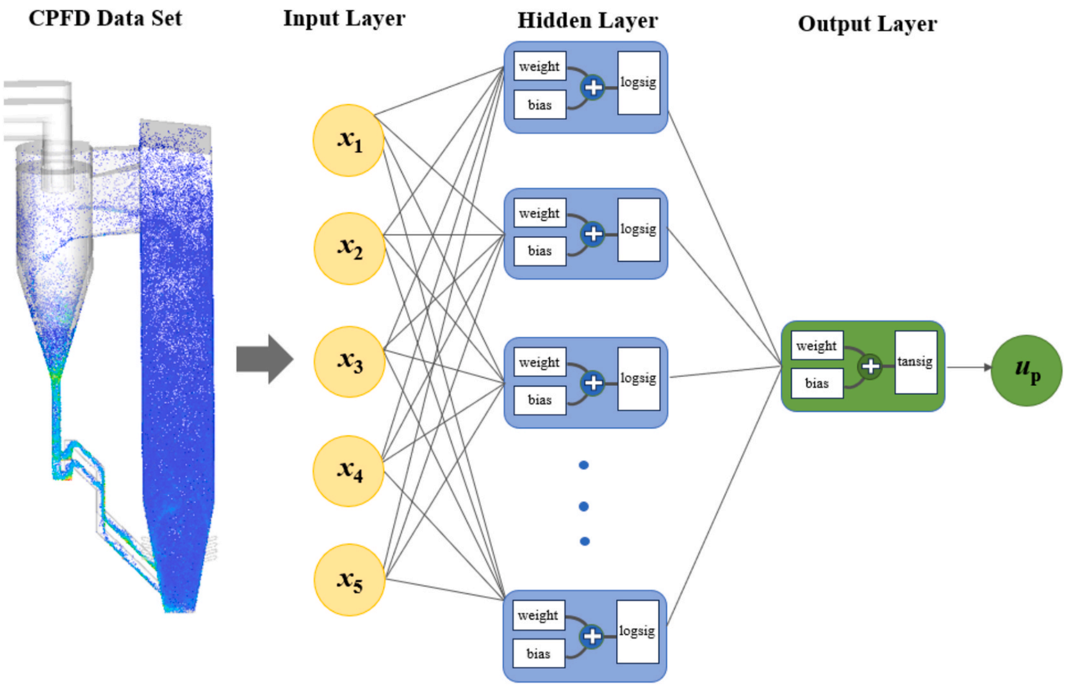

Fig. 12. Schematic diagram of the constructed GA-BP neural network.

and machine learning, to obtain a u_p prediction model that applies to a wide range of working conditions and the whole domain.

4.2. Theoretical calculation model

For the gas–solid two-phase flow, the drag force mainly drives the particle lateral movement, and the Newtonian motion equation of the particles is expressed as follows:

$$\frac{du_p}{dt} = D(u_g - u_p) \tag{12}$$

It can be further converted into Eq. (13):

$$\frac{du_p}{dx} \cdot u_p = D(u_g - u_p) \tag{13}$$

Re_p in a CFB boiler furnace is mainly in the range of 0.5–1000, so the corresponding drag function D can be written as follows (Gidaspow, 1994):

$$D = \frac{9}{2} \cdot \frac{\mu_g \varepsilon_g^{-2.65}}{\rho_p r_p^2} + \frac{27}{20} \cdot \frac{\rho_g \varepsilon_g^{-2.65} \left| u_g - u_p \right|^{0.687}}{\rho_p r_p} \tag{14}$$

Substituting Eq. (14) into Eq. (13) gives the following equation:

$$\frac{u_p}{u_g - u_p} du_p = D dx = \left(\frac{9}{2} \cdot \frac{\mu_g \varepsilon_g^{-2.65}}{\rho_p r_p^2} + \frac{27}{20} \cdot \frac{\rho_g \varepsilon_g^{-2.65} \left| u_g - u_p \right|^{0.687}}{\rho_p r_p} \right) dx \tag{15}$$

Eq. (15) is a first-order linear non-homogeneous differential equation. For the right side of the equation, considering that the second term contains the absolute value of the variable u_p, no analytical solution can be obtained if it is solved directly. Therefore, in this paper, the whole term $\left| u_g - u_p \right|^{0.687}$ is regarded as a new variable α for simplification, and the differential equation is solved as follows:

$$- u_g \ln(u_g - u_p) - u_p = \left(\frac{9}{2} \cdot \frac{\mu_g \varepsilon_g^{-2.65}}{\rho_p r_p^2} + \frac{27}{20} \cdot \frac{\rho_g \varepsilon_g^{-2.65} \alpha}{\rho_p r_p} \right) x + C \tag{16}$$

This equation is an implicit function of u_p, in which the gas velocity, voidage, particle lateral position, α, and particle radius can be regarded as independent variables x_1, x_2, x_3, x_4, and x_5, respectively, as shown below. Substituting the corresponding CPFD calculation data into this equation and solving the unknown coefficients A, B, and C, the distribution expression of u_p can be obtained.

$$- x_1 \ln(x_1 - y) - y = \left(\frac{A x_2^{-2.65}}{x_5^2} + \frac{B x_2^{-2.65} x_4}{x_5} \right) x_3 + C \tag{17}$$

As discussed in Section 4.1, u_p exhibits different distribution characteristics across various regions. Therefore, for regions featured by different solid suspension densities, the coefficients in the implicit equations related to u_p are also discrepant. Table 5 provides the u_p calculation method derived from the physical model. The R_2 values of all expressions exceeded 0.9, indicating that the established model has excellent accuracy.

4.3. GA-BP neural network

4.3.1. Model structure

The computing units in ANN are called neurons. Among them, the neurons responsible for receiving external information are defined as input layer neurons, and the neurons taking charge of the output of information are called output layer neurons (Ganesan et al., 2015). A neuron calculates the weighted sum of its inputs and then passes it to the activation function to obtain the neuron output. Mathematically, the output y_k of the k_{th} neuron can be expressed as Eq. (18):

$$y_k = f(\beta_k) = f\left(\sum_{i=1}^{d} (w_{ik} x_i + b_k) \right) \tag{18}$$

where x_i are the input signals, w_{ik} are the connection weights of the neurons, f is the activation function, and b_k are the biases.

An ANN typically consists of three or more layers: the input layer, the hidden layer, and the output layer (Paliwal and Kumar, 2009). In this study, based on the relationship between each influencing factor and u_p, the input layer signals are finalized as gas velocity, voidage, particle lateral position, β, and particle radius, while the u_p is defined as the output layer signal. The hidden layer processes the input data; the more hidden layers there are, the more comprehensive the information that can be processed. However, selecting too many hidden layers may lead

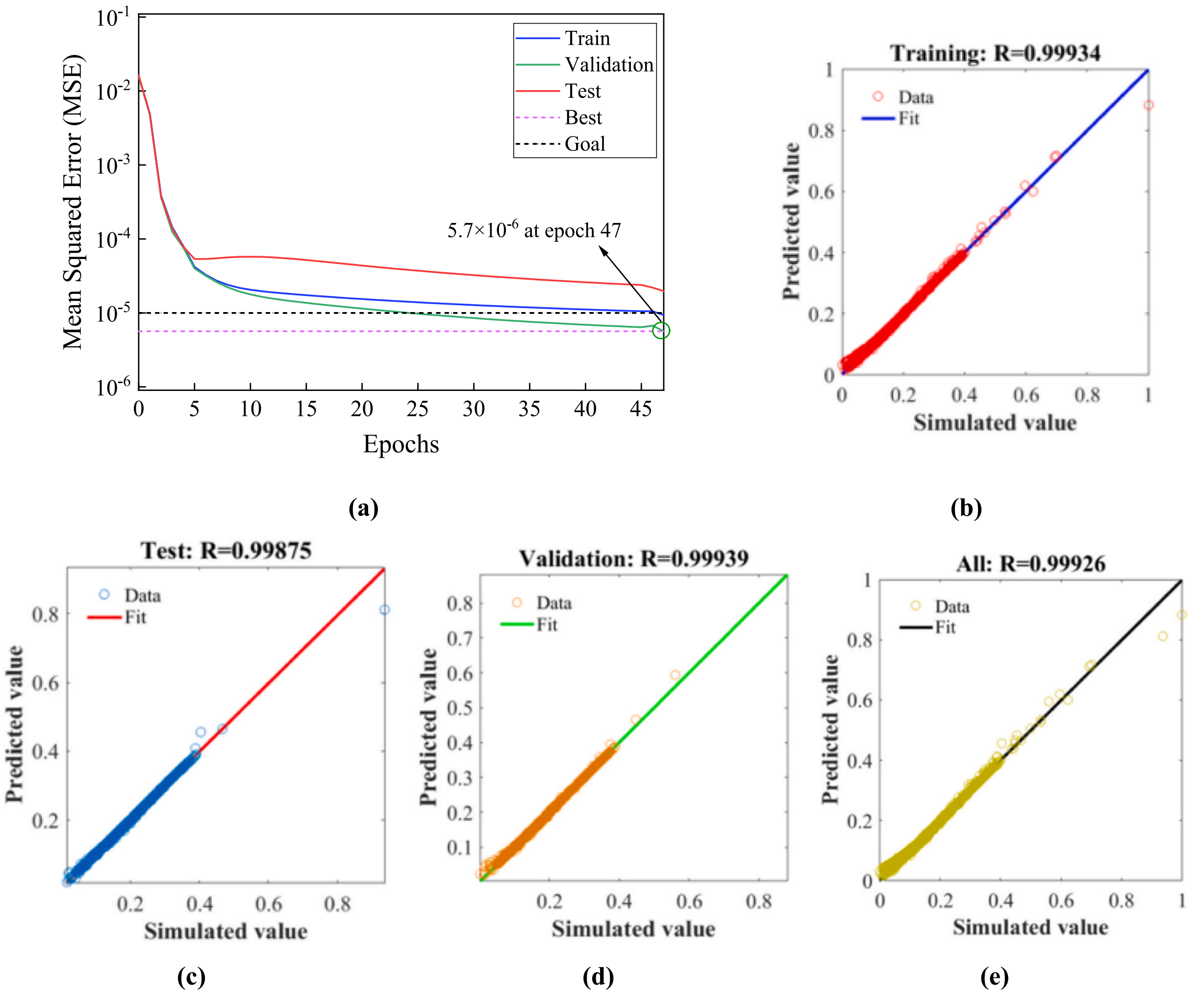

Fig. 13. Training performance of the GA-BP neural network: (a) Mean squared error (MSE) during ANN training; (b) R of the training set; (c) R of the test set; (d) R of the validation set; (e) R of all sets.

to overfitting. Generally, a neural network topology with a single hidden layer is sufficient to solve most problems. Therefore, in this study, the number of hidden layers was set to 1. For hidden layer neurons, the number q is typically determined by the following equation:

$$q = \sqrt{m+n} + a \tag{19}$$

where m and n are the number of input layer nodes and output layer nodes respectively, and a is an integer in 1–10. In this study, $q = 4$–13, so the number of hidden layer neurons is selected in 4–13.

Commonly used training algorithms in ANN include Levenberg-Marquardt (LM), scaled conjugate gradients (SCG), gradient descent with momentum, and adaptive learning rules (GDX) (Hamad et al., 2017; Shabanpour et al., 2017; Worden and Barton, 2004). Among these, the LM algorithm has a high calculation speed and learning accuracy and is used in this study to train the ANN.

The data set used in the model comes from the CPFD simulation, of which 70 % is used for training, 15 % is used for testing, and 15 % is for validation. To eliminate the effect of consistent data sequence on model training parameters, the data are randomly sorted in each training and testing stage. Additionally, to accelerate convergence, the data are normalized using Eq. (20) before training the neural network:

$$x_{\mathrm{norm}} = \frac{x - x_{\min}}{x_{\max} - x_{\min}} \tag{20}$$

where x_{norm}, $x_{\max}$, and $x_{\min}$ are the normalized, maximum, and minimum values of the input respectively.

The root mean square error (RMSE) and coefficient of determination (R_2) are used to evaluate the prediction performance of the model:

$$\mathrm{RMSE} = \sqrt{\frac{1}{N}\sum_{i=1}^{N}(y_i - f_i)^2} \tag{21}$$

$$R^2 = 1 - \frac{\sum_{i=1}^{N}(y_i - f_i)^2}{\sum_{i=1}^{N}(y_i - \overline{y}_i)^2} \tag{22}$$

where y_i and f_i are the predicted and target values, respectively; and $\overline{y}_i$ is the mean value of y_i.

Fig. 11 shows the RMSE and R_2 values of u_{p} for both the test set and training set when the number of hidden layer neurons ranged from 4 to 13. The minimum RMSE and maximum R_2 values in the test set both come from the neural network architecture with hidden layer neurons $q = 13$, demonstrating that the prediction performance is optimal under this network architecture. Therefore, q is set to 13 in this study.

The detailed information on various parameters used to construct the GA-BP neural network is summarized in Table 6, and the schematic diagram of the constructed GA-BP neural network is shown in Fig. 12.

4.3.2. *Prediction results*

Based on the previous discussion in Section 4.1, the CPFD data set is classified according to the distribution characteristics of u_{p}, and it is used

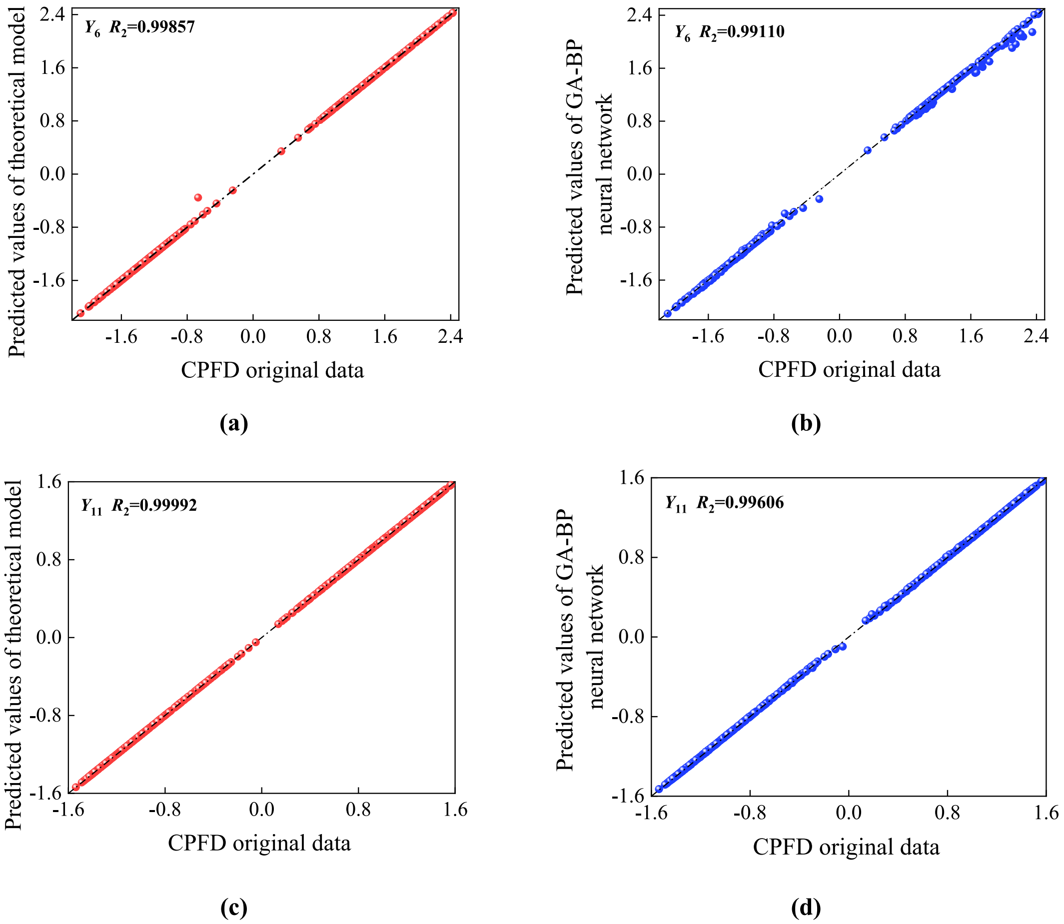

(a) (b)

(c) (d)

Fig. 14. Comparison of prediction performance between the theoretical model and GA-BP neural network: (a) u_p on Y_6 predicted by theoretical model; (b) u_p on Y_6 predicted by GA-BP neural network; (c) u_p on Y_{11} predicted by theoretical model; (d) u_p on Y_{11} predicted by GA-BP neural network.

to train the GA-BP neural network. After iteration and optimization, the connection weights, biases, and the corresponding RMSE and R_2 values are obtained and listed in Table S2 (SM). Fig. 13 illustrates the training performance of the model in predicting the particle lateral velocity distribution in the dilute phase region. It shows that the model reaches a minimum error of 5.7 × 10^{-6} after 32 iterations, satisfying the convergence requirement. Furthermore, the R_2 values for the training set, validation set, test set, and all sets exceed 0.99, indicating excellent prediction performance.

4.4. Comparison of theoretical model and GA-BP neural network model

To quantitatively characterize the u_p distribution, two models are developed based on physical model derivation and GA-BP neural network, respectively. To select an optimal model for integrating it into the two-dimensional CFB mathematical model, both methods are evaluated in terms of accuracy and applicability.

The operating performance of the boiler at 30 % load was calculated using the verified CPFD method, and the u_p distribution was obtained. Fig. 14 shows the predicted u_p on monitoring surfaces Y_6 and Y_{11} using the above two methods. Both models exhibit excellent prediction performance, with R_2 exceeding 0.99. Regarding applicability, the u_p calculation method based on the physical model is relatively simple, involving five independent variables, which has a clear physical meaning and strong universality. The GA-BP neural network reversely solves the neural network using the trained weights and biases, whose calculation process is also straightforward. However, compared to the physical model, the GA-BP neural network has a strong dependence on the data set and lacks advantages in terms of generalization and applicability to other scenarios.

Given that the theoretical calculation model based on physical functions has evident simplicity, universality, and high accuracy, it is strongly recommended to utilize this model for predicting the u_p distribution within the CFB boiler furnace. Moreover, it will be integrated into the evolving two-dimensional CFB mathematical model.

5. Conclusions

To accurately describe the lateral gas–solid flow characteristics in industrial CFB boilers, a 170 t/h CFB boiler was numerically simulated using the CPFD method validated by field test data. The lateral voidage profiles and particle lateral movement velocity distributions inside the furnace under wide operation conditions were thoroughly investigated, and simple models were developed to predict them.

When the cross-sectionally averaged voidage $\varepsilon_{gm} < 0.965$, the lateral profiles of ε_g follow a parabolic form. When $\varepsilon_{gm} \geq 0.965$, its distribution resembles a Boltzmann function, with a flat distribution of ε_g in the center region and a sharp decrease in the side wall region. Correlations for the lateral voidage profiles are proposed as follows:

$$\varepsilon_{gm} < 0.965 \quad \frac{1-\varepsilon_g}{1-\varepsilon_{gm}} = \begin{cases} a\left(\frac{x}{X}\right)^2 + b\left(\frac{x}{X}\right) + c, & -1 \leqslant \frac{x}{X} \leqslant 1 \\ a = 0.611 + e^{1.752\mathrm{Re_p}-8.425} \\ b = -0.05\mathrm{Re_p^3} + 0.50\mathrm{Re_p^2} - 1.577\mathrm{Re_p} + 1.570 \\ c = 0.402 + \frac{0.267}{1+e^{6.882\mathrm{Re_p}-30.278}} \end{cases}$$

$$\varepsilon_{gm} \geqslant 0.965 \quad \frac{1-\varepsilon_g}{1-\varepsilon_{gm}} = \begin{cases} 0.858 + \dfrac{5.651}{1+e^{24.713\left(\frac{x}{X}\right)+24.830}}, & -1 \leqslant \dfrac{x}{X} \leqslant 0 \\ 0.858 + \dfrac{5.651}{1+e^{-24.713\left(\frac{x}{X}\right)+24.830}}, & 0 < \dfrac{x}{X} \leqslant 1 \end{cases}$$

The u_p distribution in each region generally follows a parabolic distribution, with a tendency for particles to move toward the wall in dilute phase and dense phase regions, while in the transition region, it presents an obvious centripetal particle flow, thus forming a solids internal circulation. Key factors such as particle size, gas velocity, and particle concentration significantly influence the u_p. Two models of predicting u_p were established based on physical model derivation (theoretical model) and GA-BP neural network, respectively. Both models demonstrate excellent accuracy, with R_2 values exceeding 0.99. However, the theoretical model has a simpler form with clear physical meaning and a wider range of applications.

This study offers a new perspective and methodology for the quantitative characterization of lateral gas–solid flow in industrial CFB boilers. The established simple models for calculating lateral voidage and particle lateral movement velocity can be integrated into the two-dimensional CFB mathematical model. In the future, we will verify the models in this paper on two-dimensional/three-dimensional CFB test benches of different scales. In combination with combustion reactions, we will further explore the lateral non-uniformity of gas–solid flow, heat transfer, combustion, and pollutant emissions within hot-state CFBs.

CRediT authorship contribution statement

Manxia Shang: Writing – original draft, Methodology, Investigation. **Ling Jiang:** Investigation. **Li Zhao:** Writing – review & editing. **Zhong Huang:** Writing – review & editing. **Xiwei Ke:** Writing – review & editing, Methodology. **Junfu Lyu:** Writing – review & editing, Funding acquisition.

Declaration of competing interest

The authors declare that they have no known competing financial interests or personal relationships that could have appeared to influence the work reported in this paper.

Acknowledgment

This research was supported by the National Natural Science Foundation of China (No. 52306251) and the Program of Beijing Huairou Laboratory (ZD2023008A).

Appendix A. Supplementary data

Supplementary data to this article can be found online at https://doi.org/10.1016/j.ces.2025.121773.

Data availability

Data will be made available on request.

References

Andrews, M.J., O'Rourke, P.J., 1996. The multiphase particle-in-cell (MP-PIC) method for dense particulate flows. Int. J. Multiphase Flow 22 (2), 379–402. https://doi.org/10.1016/0301-9322(95)00072-0.

Bai, Z., Hu, W., Zhu, X., Wang, S., Gu, Y., 2023. Solar-driven biomass steam gasification by new concept of solar particles heat carrier with CPFD simulation. Energ Convers Manage 293, 117500. https://doi.org/10.1016/j.enconman.2023.117500.

Bai, D.R., Zhu, J.X., Jin, Y., Yu, Z.Q., 1995. Internal recirculation flow structure in vertical upflow gas-soli-ds suspensions Part I. A Core-Annulus Model. Powder Technol. 85 (2), 171–177. https://doi.org/10.1016/0032-5910(95)03010-7.

Bayham, S.C., Breault, R., Monazam, E., 2017. Applications of tribology to determine attrition by wear of particulate solids in CFB systems. Powder Technol. 316, 59–68. https://doi.org/10.1016/j.powtec.2016.10.059.

Beetstra, R., Hoef, M.A.V.D., Kuipers, J.A.M., 2007. Drag force of intermediate Reynolds number flow past mono- and bidisperse arrays of spheres. AIChE J. 53, 489–501. https://doi.org/10.1002/aic.11065.

Blaszczuk, A., Nowak, W., 2015. Heat transfer behavior inside a furnace chamber of largescale supercritical CFB reactor. Int. J. Heat Mass Tran 87, 464–480. https://doi.org/10.1016/j.ijheatmasstransfer.2015.04.037.

Breault, R.W., Weber, J., Shadle, L.J., 2020. The development of a generalized riser flow regime map based upon higher moment and chaotic statistics using electrical capacitance volume tomography (ECVT). Powder Technol. 365, 12–27. https://doi.org/10.1016/j.powtec.2019.03.036.

Cai, R.X., Zhang, H., Zhang, M., Yang, H.R., Lyu, J.F., Yue, G.X., 2018. Development and application of the design principle of fluidization state specification in CFB coal combustion. Fuel Process. Technol. 174, 41–52. https://doi.org/10.1016/j.fuproc.2018.02.009.

Chen, M.R., Chen, B.P., Zeng, G.Q., Lu, K.D., Chu, P., 2020. An adaptive fractional-order BP neural networ-k based on extremal optimization for handwritten digits recognition. Neurocomputing 391, 260–272. https://doi.org/10.1016/j.neucom.2018.10.090.

Farzaneh, M., Sasic, S., Almstedt, A.E., Johnsson, F., Pallarès, D., 2011. A novel multigrid technique for La-grangian modeling of fuel mixing in fluidized beds. Chem. Eng. Sci. 66, 5628–5637. https://doi.org/10.1016/j.ces.2011.07.060.

Ganesan, P., Rajakarunakaran, S., Thirugnanasambandam, M., Devaraj, D., 2015. Artificial neural network model to predict the diesel electric generator performance and exhaust emissions. Energy 83, 115–124. https://doi.org/10.1016/j.energy.2015.02.094.

Gidaspow, D., 1994. Multiphase flow and fluidization: Continuum and kinetic theory description. Academic Press, New York.

Gungor, A., Eskin, N., 2007. Hydrodynamic modeling of a circulating fluidized bed. Powder Technol. 172 (1), 1–13. https://doi.org/10.1016/j.powtec.2006.10.035.

Gungor, A., Eskin, N., 2008. Two-dimensional coal combustion modeling of CFB. Int. J. Therm. Sci. 47 (2), 157–174. https://doi.org/10.1016/j.ijthermalsci.2007.01.017.

Hamad, K., Khalil, M.A., Shanableh, A., 2017. Modeling roadway traffic noise in a hot climate using artificial neural networks. Transp. Res. D-Transp. Environ. 53, 161–177. https://doi.org/10.1016/j.trd.2017.04.014.

S.E. Harris, D.G. Crighton, Solitons, solitary waves, and voidage disturbances in gas-fluidized beds, J. Fluid Mech. 266 (1994) 243-276, https://doi.org/ 10.1017/S0022112094000996.

Hartge, E.U., Rensner, D., Werther, J., 1988. Solids concentration and velocity patterns in circulating fluidized beds. In: Basu, P., Large, J.F. (Eds.), Circulating Fluidized Bed Technology II. Pergamon, Oxford, pp. 165–180.

Hensler, T., Firsching, M., Bonilla, J.S.G., Wörlein, T., Uhlmann, N., Wirth, K.E., 2016. Non-invasive investigation of the cross-sectional solids distribution in CFB risers by X-ray computed tomography. Powder Technol. 297, 247–258. https://doi.org/10.1016/j.powtec.2016.04.030.

Herb, B., Tuzla, K., Chen, J.C., 1989. Distribution of solid concentrations in circulating fluidized bed. In: Grace, J.R., Shemilt, L.W., Bergougnou, M.A. (Eds.), Fluidization VI. Engineering Foundation, New York, pp. 65–72.

Herbert, P.M., Gauthier, T.A., Briens, C.L., Bergougnou, M.A., 1998. Flow study of a 0.05 m diameter downflow circulating fluidized bed. Powder Technol. 96, 255–261. https://doi.org/10.1016/S0032-5910(97)03381-0.

Huang, X.K., Bai, Z., Zhu, X.L., Wang, S.S., Mu, L., Gong, L., 2025. Gas-solid flow, combustion characteristics, and gas emissions in a 75 t/h CFB boiler based on the CPFD method. J. Therm. Sci 34 (1), 323–336. https://doi.org/10.1007/s11630-025-2092-7.

Issangya, A.S., Grace, J.R., Zhu, J.X., 2005. Bottom and exit region solids hold-ups in circulating fluidized bed risers. In: Cen, K. (Ed.), Circulating Fluidized Bed Technology VIII. International Academic Publishers, Hangzhou, pp. 209–215.

Jin, Y., Lu, X.F., Song, Y.F., Zheng, X., Lei, X.J., Liu, Z., Fan, X.C., Liu, C.C., 2021. A comprehensive understanding of the non-uniform characteristics and regulation mechanism of six external loops in a 600 MW supercritical CFB boiler. Energy 222, 120032. https://doi.org/10.1016/j.energy.2021.120032.

Ke, X.W., Yao, Y.G., Huang, Z., Zhang, M., Lyu, J.F., Yang, H.R., Zhou, T., 2022. Prediction and minimization of NO_x emission in a circulating fluidized bed combustor: Improvement of bed quality by optimizing cyclone performance and coal particle size. Fuel 328, 125287. https://doi.org/10.1016/j.fuel.2022.125287.

Kim, S.W., Kirbas, G., Bi, X., Lim, C.J., Grace, J.R., 2004. Flow structure and thickness of annular downflo-w layer in a circulating fluidized bed riser. Powder Technol. 142 (1), 48–58. https://doi.org/10.1016/j.powtec.2004.03.011.

Klimanek, A., Bigda, J., 2018. CFD modeling of CO_2 enhanced gasification of coal in a pressurized circulating fluidized bed reactor. Energy 160, 710–719. https://doi.org/10.1016/j.energy.2018.07.046.

Koeninger, B., Hensler, T., Schug, S., Arlt, W., Wirth, K.E., 2017. Horizontal secondary gas injection in flui-dized beds: Solid concentration and velocity in multiphase jets. Powder Technol. 316, 49–58. https://doi.org/10.1016/j.powtec.2017.01.057.

Kruse, M., Schoenfelder, H., Werther, J., 1995. A two-dimensional model for gas mixing in the upper dilute zone of a circulating fluidized bed. Can. J. Chem. Eng. 73, 620–634. https://doi.org/10.1002/cjce.5450730505.

Kruse, M., Werther, J., 1995. 2D gas and solids flow prediction in circulating fluidized beds based on suction probe and pressure profile measurements. Chem. Eng. Process. 34, 185–203. https://doi.org/10.1016/0255-2701(94)04004-4.

Krzywanski, J., Czakiert, T., Blaszczuk, A., Rajczyk, R., Muskala, W., Nowak, W., 2015. A generalized model of SO_2 emissions from large- and small-scale CFB boilers by artificial neural network approach Part 2. SO_2 emissions from large- and pilot-scale

CFB boilers in O_2/N_2, O_2/CO_2 and O_2/RFG combustion atmospheres. Fuel Process. Technol. 139, 73–85. https://doi.org/10.1016/j.fuproc.2015.08.009.

Lee, B.H., Kim, K.M., Bae, Y.H., Oh, H.S., Kim, G.B., Jeon, C.H., Ahn, Y.H., 2022. Effect of bed particle size on the gas-particle hydrodynamics and wall erosion characteristics in a 550 MWe USC CFB boiler using CPFD simulation. Energy 254, 124263. https://doi.org/10.1016/j.energy.2022.124263.

Liu, H.P., Sun, H.W., Bi, Y., Jia, C.X., Zhang, L., Li, Y.L., Qin, H., Wang, Q., 2023. Effect of secondary air on NO emission in a 440 t/h circulating fluidized bed boiler based on CPFD method. Particuology 83, 18–31. https://doi.org/10.1016/j.partic.2023.02.002.

Liu, X.D., Zhang, H., Yang, H.R., Zhang, Y., Lyu, J.F., 2023. Validation and evaluation of the CPFD modeling of dense particle flow velocity: Taking particle flow around an obstacle as an example. Chem. Eng. J. 453, 139719. https://doi.org/10.1016/j.cej.2022.139719.

Ma, Q., Lei, F.L., Xiao, Y.H., 2018. Numerical analysis of operating conditions for establishing high densit-y circulating fluidized bed by CPFD method. Powder Technol. 338, 446–457. https://doi.org/10.1016/j.powtec.2018.07.012.

Ma, X.Y., Wang, D.X., Liu, B., Dong, H., Zhao, L., 2023. Numerical simulations and validation of gas–solid flows in a fluidized-bed roaster based on the CFD-DPM model. Can. J. Chem. Eng. 101 (11), 6577–6590. https://doi.org/10.1002/cjce.24904.

Metzger, J.P., Chen, B.Y., Penn, A., Guenthner, C., Pruessmann, K.P., Müller, C.R., 2024. Magnetic resonance velocimetry of particle hydrodynamics in a three-dimensional draft tube spout-fluid bed. Chem. Eng. J. 485, 149678. https://doi.org/10.1016/j.cej.2024.149678.

Namkung, W., Sang, D.K., 2000. Radial gas mixing in a circulating fluidized bed. Powder Technol. 113, 23–29. https://doi.org/10.1016/S0032-5910(99)00288-0.

X.H. Ni, Z. Yang, Inverter fault diagnosis based on BP neural network, in: Proceedings of 2021 6th International Conference on Automation, Control and Robotics Engineering (CACRE), Dalian, China, 2021, pp. 203-208.

Nowak, W., 2003. Clean coal fluidized-bed technology in Poland. Appl. Energy 74, 405–413. https://doi.org/10.1016/S0306-2619(02)00195-2.

Paliwal, M., Kumar, U.A., 2009. Neural networks and statistical techniques: a review of applications. Expert Syst. Appl. 36, 2–17. https://doi.org/10.1016/j.eswa.2007.10.005.

Paliwal, M., Kumar, U.A., 2009. Neural networks and statistical techniques: a review of applications. Expert Syst. Appl. 36 (1), 2–17. https://doi.org/10.1016/j.eswa.2007.10.005.

Pallarès, D., Johnsson, F., 2006. A novel technique for particle tracking in cold 2-dimensional fluidized beds-simulating fuel dispersion. Chem. Eng. Sci. 61, 2710–2720. https://doi.org/10.1016/j.ces.2005.11.030.

Parssinen, J.H., Zhu, J.X., 2001. Particle velocity and flow development in a long and high-flux circulating fluidized bed riser. Chem. Eng. Sci. 56 (18), 5295–5303. https://doi.org/10.1016/S0009-2509(01)00200-7.

Patience, G.S., Chaouki, J., 1996. Solids hydrodynamics in the fully developed region of CFB risers. In: Large, J.F., Laguerie, C. (Eds.), Fluidization VIII. Engineering Foundation, New York, pp. 33–40.

Scala, F., 2018. Particle agglomeration during fluidized bed combustion: Mechanisms, early detection and possible countermeasures. Fuel Process. Technol. 171, 31–38. https://doi.org/10.1016/j.fuproc.2017.11.001.

Schoenfelder, H., Kruse, M., Werther, J., 1996. Two-dimensional model for circulating fluidized-bed reactors. AIChE J. 42 (7), 1875–1888. https://doi.org/10.1002/aic.690420709.

Sedighi, R., Meiabadi, M.S., Sedighi, M., 2017. Optimisation of gate location based on weld line in plastic injection moulding using computer-aided engineering, artificial neural network, and genetic algorithm. Int. J. Automot. Mech. Eng. 14 (3), 4419–4431. https://doi.org/10.15282/ijame.14.3.2017.3.0350.

Shabanpour, H., Yousefi, S., Saen, R.F., 2017. Forecasting efficiency of green suppliers by dynamic data envelopment analysis and artificial neural networks. J. Cleaner Prod. 142, 1098–1107. https://doi.org/10.1016/j.jclepro.2016.08.147.

Shaffer, F., Gopalan, B., Breault, R.W., Cocco, R., Karri, S.B.R., Hays, R., Knowlton, T., 2013. High speed i-maging of particle flow fields in CFB risers. Powder Technol. 242, 86–99. https://doi.org/10.1016/j.powtec.2013.01.012.

Shang, M.X., Yao, Y.G., Ke, X.W., Huang, Z., Zhou, T., Lyu, J.F., 2024. Effect of back pressure on gas-solid distribution characteristics of cyclone distributor applied in powdered coal-fired circulating fluidized bed combustion system. Powder Technol. 431, 119039. https://doi.org/10.1016/j.powtec.2023.119039.

Singh, P., Dwivedi, P., Kant, V., 2019. A hybrid method based on neural network and improved environmental adaptation method using Controlled Gaussian Mutation with real parameter for short-term load forecasting. Energy 174, 460–477. https://doi.org/10.1016/j.energy.2019.02.141.

Snider, D.M., 2001. An incompressible three-dimensional multiphase particle-in-cell model for dense particle flows. J. Comput. Phys. 170 (2), 523–549. https://doi.org/10.1006/jcph.2001.6747.

Snider, D.M., O'Rourke, P.J., Andrews, M.J., 1998. Sediment flow in inclined vessels calculated using a multiphase particle-in-cell model for dense particle flows. Int. J. Multiphase Flow 24, 1359–1382. https://doi.org/10.1016/S0301-9322(98)00030-5.

Song, G.L., Yang, Z., Zhou, T., Lyu, Q.G., 2018. Operating technical characteristics on asymmetrical arrangement of six cyclones in a 600 MW supercritical CFB boiler. Appl. Therm. Eng. 143, 236–247. https://doi.org/10.1016/j.applthermaleng.2018.07.101.

Tribedi, T., Tiwari, P., Pant, H.J., Upadhyay, R.K., 2023. Solid flow mapping at the bottom section of a pilot-plant scale riser with the help of a radioactive particle tracking technique. Ind. Eng. Chem. Res. 62, 19133–19144. https://doi.org/10.1021/acs.iecr.3c00788.

Tung, Y., Li, J., Kwauk, M., 1988. Radial voidage profile in a fast fluidized bed. In: Kwauk, M., Kunii, D. (Eds.), Fluidization 88: Science and Technology. Science Press, Beijing, pp. 139–145.

Valente, G.F.S., Mendonça, R.C.S., Pereira, J.A.M., Felix, L.B., 2014. Artificial neural network prediction of chemical oxygen demand in dairy industry effluent treated by electrocoagulation. Sep. Purif. Technol. 132, 627–633. https://doi.org/10.1016/j.seppur.2014.05.053.

Wang, Y., Wei, F., Wang, Z.W., Jin, Y., Yu, Z.Q., 1998. Radial profiles of solids concentration and velocity in a very fine particle (36 μm) riser. Powder Technol. 96 (3), 262–266. https://doi.org/10.1016/S0032-5910(97)03382-2.

Weber, J.M., Bobek, M.M., Breault, R.W., Mei, J.S., Shadle, L.J., 2018. Investigation of core-annular flow in an industrial scale circulating fluidized bed riser with electrical capacitance volume tomography (ECVT). Powder Technol. 327, 524–535. https://doi.org/10.1016/j.powtec.2017.12.094.

Wei, F., Lin, H.F., Cheng, Y., Wang, Z.W., Jin, Y., 1998. Profiles of particle velocity and solids fraction in a high-density riser. Powder Technol. 100, 183–189. https://doi.org/10.1016/S0032-5910(98)00139-9.

Weinstein, H., Shao, M., Schnitzlein, M., 1985. Radial variation in solid density in high velocity fluidization. In: Basu, P. (Ed.), Circulating Fluidized Bed Technology I. Pergamon, Toronto, pp. 201–205.

Wen, C.Y., Yu, Y.H., 1966. Mechanics of fluidization. Chem. Eng. Prog., Symp. Ser. 62, 100–111.

White, F.M., 1991. Viscous fluid flow. McGraw-Hill, New York.

Wong, R., Pugsley, T., Berrut, F., 1992. Modeling the axial voidage profile and flow structure in risers of circulating fluidized beds. Chem. Eng. Sci. 47 (9–11), 2301–2306. https://doi.org/10.1016/0009-2509(92)87051-Q.

Worden, K., Barton, J.M.D., 2004. An overview of intelligent fault detection in systems and structures. Struct. Health Monit. 3 (1), 85–98. https://doi.org/10.1177/1475921704041866.

Xu, J., Lu, X.F., Zhang, W.Q., Chen, J.B., Wang, Q.H., Chen, Y., Guo, Q., 2018. Effects of superficial gas velocity and static bed height on gas-solid flow characteristics in a 60-meter-high transparent CFB riser. Chem. Eng. J. 334, 545–557. https://doi.org/10.1016/j.cej.2017.09.131.

Xu, G.W., Sun, G.G., Nomura, K., Li, J.H., Kato, K., 1999. Two distinctive variational regions of radial particle concentration profiles in circulating fluidized bed risers. Powder Technol. 101, 91–100. https://doi.org/10.1016/S0032-5910(98)00157-0.

Xu, G.W., Sun, G.G., Gao, S.Q., 2004. Estimating radial voidage profiles for all fluidization regimes in circulating fluidized bed risers. Powder Technol. 139, 186–192. https://doi.org/10.1016/j.powtec.2003.10.014.

Yan, J., Lu, X.F., Xue, R., Lu, J.Y., Zheng, Y., Zhang, Y., Liu, Z., 2020. Validation and application of CPFD model in simulating gas-solid flow and combustion of a supercritical CFB boiler with improved inlet boundary conditions. Fuel Process. Technol. 208, 106512. https://doi.org/10.1016/j.fuproc.2020.106512.

Yang, S.L., Wan, Z.H., Wang, S., Wang, H., 2021. Reactive MP-PIC investigation of heat and mass transfer behaviors during the biomass pyrolysis in a fluidized bed reactor. J. Environ. Chem. Eng. 9, 105047. https://doi.org/10.1016/j.jece.2021.105047.

Zhang, Y.F., Arastoopour, H., 1995. Dilute fluidized cracking catalyst particles-gas-flow behavior in the riser of a circulating fluidized bed. Powder Technol. 84, 221–229. https://doi.org/10.1016/0032-5910(95)02991-A.

Zhang, W., Tung, Y., Johnsson, F., 1991. Radial voidage profiles in fast fluidized beds of different diameters. Chem. Eng. Sci. 46, 3045–3052. https://doi.org/10.1016/0009-2509(91)85008-L.

Zhou, C.G., Jonasson, C., Gullberg, M., Ahrentorp, F., Johansson, C., 2024. Application of the magnetic tracer-tracking system in solids circulation measurement in a fluidized bed standpipe. Chem. Eng. J. 498, 155030. https://doi.org/10.1016/j.cej.2024.155030.

Zhu, X.L., Li, C.Y., Yang, C.H., Wang, G.W., Geng, Q., Li, T., 2013. Gas-solids flow structure and prediction of solids concentration distribution inside a novel multi-regime riser. Chem. Eng. J. 232, 290–301. https://doi.org/10.1016/j.cej.2013.06.126.

Zhu, X.L., Dong, P.F., Tu, Q.Y., Zhu, Z.P., Yang, W.Q., Wang, H.G., 2020. Investigation of gas-solids flow characteristics in a pressurised circulating fluidised bed by experiment and simulation. Powder Technol. 366, 420–433. https://doi.org/10.1016/j.powtec.2020.02.047.

Zhu, H.Y., Zhu, J., 2008. Characterization of fluidization behavior in the bottom region of CFB risers. Chem. Eng. J. 141, 169–179. https://doi.org/10.1016/j.cej.2007.12.015.